Earth and Planetary Science Letters 584 (2022) 117442

Contents lists available at ScienceDirect

Earth and Planetary Science Letters

www.elsevier.com/locate/epsl

On the scale dependence in the dynamics of frictional rupture: Constant fracture energy versus size-dependent breakdown work

Federica Paglialunga [a,*], François X. Passelègue [a], Nicolas Brantut [b], Fabian Barras [c], Mathias Lebihain [a,d], Marie Violay [a]

[a] Laboratoire de Mécanique des Roches, École Polytechnique Fédérale de Lausanne, Switzerland
[b] Department of Earth Sciences, University College London, London, UK
[c] NJORD Centre for Studies of the Physics of the Earth, University of Oslo, Norway
[d] Ecole Nationale des Ponts et Chaussées, Laboratoire Navier, Champs-sur-Marne, France

ARTICLE INFO

Article history:
Received 30 April 2021
Received in revised form 10 February 2022
Accepted 14 February 2022
Available online 17 March 2022
Editor: R. Bendick

Dataset link: https://doi.org/10.5281/zenodo.6200886

Keywords:
rupture dynamics
earthquake energy budget
fracture energy
breakdown work
frictional rupture

ABSTRACT

Potential energy stored during the inter-seismic period by tectonic loading around faults is released during earthquakes as radiated energy, frictional dissipation and fracture energy. The latter is of first importance since it is expected to control the nucleation, the propagation and the arrest of the seismic rupture. On one side, the seismological fracture energy estimated for natural earthquakes (commonly called breakdown work) ranges between 1 J/m^2 and tens of MJ/m^2 for the largest events, and shows a clear slip dependence. On the other side, recent experimental studies highlighted that, concerning rupture experiments, fracture energy is a material property (energy required to break the fault interface) independently of the size of the event, i.e. of the seismic slip. To reconcile these contradictory observations and definitions, we performed stick-slip experiments, as analog for earthquakes, in a bi-axial shear configuration. We estimated fracture energy through both Linear Elastic Fracture Mechanics (LEFM) and a Cohesive Zone Model (CZM) and through the integration of the near-fault stress-slip evolution. We show that, at the scale of our experiments, fault weakening is divided into a near-tip weakening, corresponding to an energy of few J/m^2, consistent with the one estimated through LEFM and CZM, and a long-tailed weakening corresponding to a larger energy not localized at the rupture tip, increasing with slip. Through numerical simulations, we demonstrate that only near-tip weakening controls the rupture initiation and that long-tailed weakening can enhance slip during rupture propagation and allow the rupture to overcome stress heterogeneity along the fault. We conclude that the origin of the seismological estimates of breakdown work could be related to the energy dissipated in the long-tailed weakening rather than to the one dissipated near the tip.

1. Introduction

Earthquakes are due to the abrupt release of part of the elastic stored energy accumulated during the inter-seismic period, which is released as radiated energy in the bulk and dissipated energy in the vicinity of the fault. The latter can be subdivided into two contributions: (1) the so-called breakdown work, which is associated to fault weakening down to some minimum frictional strength (Tinti et al., 2005), and (2) the remaining frictional dissipation (Kanamori, 1977; Kanamori and Brodsky, 2004). The breakdown work (W_b) is a collective dissipation term that includes on- and off-fault processes occurring at a range of timescales during rupture, from the onset (i.e., near the tip of the propagating rupture) to the later stages of slip (i.e., far from the tip). Inspired from the energy budget of slip-weakening models of earthquakes (e.g., Palmer and Rice, 1973), breakdown work (previously commonly known as 'seismological' fracture energy) is often proposed as a proxy for the fracture energy (G_c) (Venkataraman and Kanamori, 2004; Abercrombie and Rice, 2005), defined as the energy consumed at the rupture tip to propagate the rupture by a unit area. However, breakdown work is analogous to fracture energy only if the fault weakening is concentrated near the propagating tip of the rupture, which is not expected to be systematically the case during natural earthquakes (e.g., Lambert and Lapusta, 2020; Brener and Bouchbinder, 2021). How this dissipated energy is distributed around the propagating rupture has a key impact on its dynamics.

Estimating the partitioning of breakdown work between fracture energy and frictional dissipation and its spatio-temporal dis-

* Corresponding author.
E-mail address: federica.paglialunga@epfl.ch (F. Paglialunga).

https://doi.org/10.1016/j.epsl.2022.117442

tribution during earthquakes is of first importance since they seem to control the nucleation and propagation of the seismic rupture, as well as the intensity of the wave radiation at the origin of ground motions. To clarify our terminology, in this paper we follow Tinti et al. (2005) and make a distinction between what we will call the breakdown work, which is defined as the total energy dissipated in excess of the residual friction, and the fracture energy (termed "surface energy" by Tinti et al. (2005)), defined as the critical energy release rate required to expand the rupture. As noted by Tinti et al. (2005), fracture energy is likely a small part of the breakdown work: this is what we explore here.

Unfortunately, most seismological observations do not allow for a complete estimate of the energy balance of crustal earthquakes, due to the presence of several unknowns, such as the stresses acting on the fault and the minimum slip distance needed to release the stress drop. The analysis of the radiated seismic waves provides a good estimate of the radiated energy (Kanamori, 1977; Venkataraman and Kanamori, 2004), but quantifying the breakdown work of earthquakes remains challenging and relies on a number of simplifying assumptions that are difficult to assess. Still today inverting the dynamic parameters controlling rupture processes during natural earthquakes requires highly instrumented fault zones (Twardzik et al., 2014). For this reason, breakdown work is often estimated from kinematic models with limited frequency bands, or constraining a priori a given weakening law, with the possibility of influencing the final values. With this in mind, such estimates indicate that 'seismological' fracture energy scales with earthquake slip, as a power law with an exponent ranging from 0.5 to 2 (e.g., Abercrombie and Rice, 2005; Viesca and Garagash, 2015).

Laboratory studies have brought useful constraints on the energetics of shear ruptures (e.g., Johnson and Scholz, 1976; Ohnaka and Yamashita, 1989; Rubinstein et al., 2004; Svetlizky and Fineberg, 2014; Bayart et al., 2016; Xu et al., 2019). Stick-slip experiments conducted on rocks or analog materials have shown that the onset of frictional slip can be described by a shear crack (i.e., mode II fracture) nucleating and propagating along the fault interface. Using Linear Elastic Fracture Mechanics (LEFM), recent studies (e.g., Svetlizky and Fineberg, 2014; Bayart et al., 2016; Kammer and McLaskey, 2019) have highlighted that the stress field and associated release of elastic energy at the rupture tip is fully controlled by a fracture energy that is a scale-independent interface property. Such estimates are found to be a fraction of the mode I fracture energy of the intact material (1 to 10 kJ/m^2), dependently on the interface properties (Svetlizky and Fineberg, 2014). For dry interfaces, such estimates can be related to the tensile fracture energy of the intact material (1 to 10 kJ/m^2) using the real area of contact broken by the frictional rupture (Svetlizky and Fineberg, 2014). Yet, this direct relation to the fracture energy of the bare material fades with more complex interface conditions (e.g. after lubrication (Bayart et al., 2016)). In addition, the propagation and arrest of dynamic ruptures in laboratory samples has been shown to be fully described by fracture mechanics (Kammer et al., 2015; Bayart et al., 2016; Galis et al., 2017; Svetlizky and Fineberg, 2014; Passelègue et al., 2020), raising the hope of predicting earthquake motions.

However, laboratory studies on *rupture* experiments have shown values of fracture energy of the order of tenths to hundreds of J/m^2 (Svetlizky and Fineberg, 2014; Kammer and McLaskey, 2019; Ohnaka, 2003), far from those of natural earthquakes, suggesting a difference between the processes included at the two scales of observations. Indeed, at the scale of natural faults, seismological observations indicate a slip-dependence of the breakdown work of earthquakes (Abercrombie and Rice (2005); Venkataraman and Kanamori (2004); Viesca and Garagash (2015); Causse et al. (2014); Tinti et al. (2005) and therein) with values ranging from 1 J/m^2 to tens of MJ/m^2 for the largest crustal earthquakes (i.e. three to four order of magnitude larger than the fracture energy of intact material constituting the seismogenic crust), differing from the notion of fracture energy as a constant material property. Recent work by Ke et al. (2020, 2022) suggests that apparent scale-dependent breakdown work can emerge in ruptures governed by an underlying constant (material-dependent) fracture energy when earthquakes propagate into regions of decreasing background stress, where ruptures progressively stop. Such apparent scaling arises due to stress drop heterogeneity rather than intrinsic fault strength evolution.

By contrast with laboratory *rupture* experiments, *friction* experiments at high slip velocity, aimed at characterizing the evolution of frictional strength that would be observed at a single point along the fault during seismic slip and have reproduced the slip-dependence of breakdown work, with values ranging between 1 kJ/m^2 to 10 MJ/m^2 (Nielsen et al., 2016; Cornelio et al., 2020; Seyler et al., 2020; Passelègue et al., 2016). Similarly, fault models based on weakening mechanisms such as thermal pressurization (Viesca and Garagash, 2015; Lambert and Lapusta, 2020) or flash heating (Brantut and Viesca, 2017) have also been shown to exhibit such scaling between slip and breakdown work. In both friction experiments and models, most of the total dissipated energy is converted into frictional dissipation, further enhancing the weakening of the fault during coseismic slip due to the occurrence of thermally activated weakening processes. In this regard Lambert and Lapusta (2020) emphasize how, due to this enhanced fault weakening prolonged after rupture propagation, breakdown work does not solely correspond to dissipation occurring within a small region near the propagating rupture tip (cohesive zone), but includes possibly large contributions from dissipation occurring at large distances from it. The exact role of such "long-tailed" weakening in the dynamics of rupture propagation, and in particular its possible contribution to fracture energy at the propagating tip, remains somewhat unclear. Using rate-and-state models of friction, recent works show that while the dynamics of the frictional rupture can be described by fracture mechanics, the fracture energy inverted at the crack tip only corresponds to a small fraction of the breakdown work integrated during rupture (Barras et al., 2020; Brener and Bouchbinder, 2021).

In this paper, we combine, in a single experimental setup, the study of rupture dynamics and friction evolution. From the variation of frictional stress with slip measured in the wake of the rupture, we show that the fracture energy represents only a small fraction of the total breakdown work at the scale of laboratory experiments, as discussed already in Tinti et al. (2005) and Cocco and Tinti (2008). Building on these observations, this manuscript tackles two objectives: firstly, to investigate and quantify the discrepancy between fracture energy and breakdown work existing at the scale of laboratory experiments, and secondly to discuss how the observed dynamics can be up-scaled to understand the energy budget of natural earthquakes.

2. Methods

2.1. Apparatus and loading conditions

Experiments were performed with a bi-axial shear apparatus, located at the Experimental Rock Mechanics Laboratory of the Swiss Federal Institute of Technology in Lausanne (EPFL). The apparatus is composed of a rigid steel frame holding two rectangular cuboid blocks of polymethylmethacrylate (PMMA) of known elastic properties (Young's modulus E=5.7 GPa and Poisson's ratio ν=0.33) (Fig. 1a.). The dimensions of the PMMA blocks are of 20 cm × 10 cm × 1 cm for the upper block, and 50 cm × 10 cm × 3 cm for the lower block, resulting in a 20 cm × 1 cm fault interface.

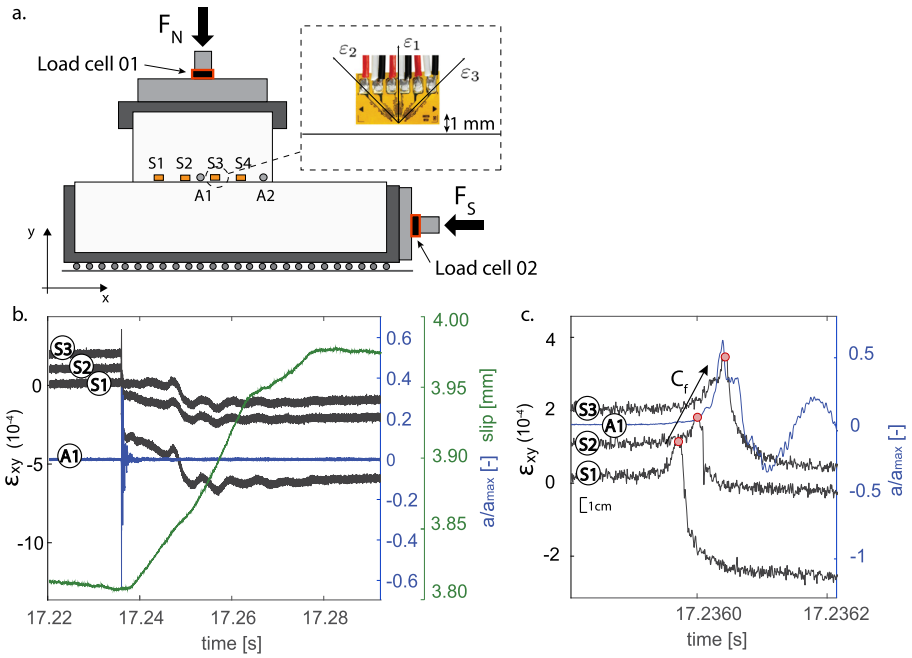

Fig. 1. a. Sketch of the biaxial apparatus used to perform stick-slip experiments. Symbols as rectangles and circles represent respectively strain gauges and accelerometers placed at a distance of 1 mm from the fault. The sketch does not respect the real distance between them, which is shown in (c). b. Evolution of strain (in black) during the occurrence of a rupture event. Strain is measured through strain gauge rosettes placed at three different locations along the fault. Macroscopic slip evolution measured through laser displacement sensor (in green). Macroscopic slip is initiated once rupture has propagated all the way through the fault. The acceleration evolution (in blue) shows radiation occurring mainly during rupture propagation and dissipating as macroscopic slip occurs. c. Zoom-in of strain and acceleration distributions during the rupture event. Rupture arrival times for each strain rosette (in red) used to estimate the rupture velocity (C_f). (For interpretation of the colors in the figure(s), the reader is referred to the web version of this article.)

External loading is imposed by using two hydraulic pumps applying respectively normal and shear load with a maximum stress of 20 MPa (Fig. 1a). The applied macroscopic loads were measured using two load cells located between the frame and the pistons, and recorded at 100 Hz sampling rate with a National Instrument data acquisition system. To capture the details of the dynamic ruptures, the upper PMMA block was equipped with an equally spaced array of strain gauge rosettes placed 1 mm away from the fault, which guaranteed high frequency measurement of strain (for details on the acquisition system refer to the Supplementary Material). To reproduce earthquakes with our experimental system, a normal load was first imposed along the fault, for values ranging between 0.2 and 5 MPa. Then, the shear load was manually increased up to the onset of instability, which resulted in a spontaneous fast release of stress along the experimental fault, associated with seismic slip and elastic wave radiation (i.e., stick slip events).

2.2. Estimation of local strain and rupture velocity

During stick-slip events, the local material response was analyzed using the strain gauge array. Denoting x and y the fault-parallel and the fault-perpendicular coordinates, respectively, the elements $\varepsilon_{xx}, \varepsilon_{yy}, \varepsilon_{xy}$ of the strain tensor were obtained from the measured strain (referred to as $\varepsilon_1, \varepsilon_2, \varepsilon_3$ for strain gauges oriented at 90°, 45° and 135° from the fault direction, respectively) as

$$\begin{aligned} \varepsilon_{yy} &= \varepsilon_1, \\ \varepsilon_{xy} &= \frac{\varepsilon_3 - \varepsilon_2}{2}, \\ \varepsilon_{xx} &= \varepsilon_3 + \varepsilon_2 - \varepsilon_1. \end{aligned} \tag{1}$$

Typical time series of shear strain (ε_{xy}) computed at each rosette location, together with the laser displacement sensor and the acceleration motions, during a stick-slip instability (here obtained at 2.3 MPa normal stress) are presented in Fig. 1b.

Rupture velocity (C_f) was estimated using the times at which the passage of rupture front was detected from the different strain gauges and the relative distance between them. The arrival of the rupture front was determined as the moment at which the strain gauges signal reached its peak (Fig. 1c); this method assumes that the rupture velocity is constant over the distance spanned by the gauge array. An increase in rupture velocity is observed with an increase in the initial peak shear stress, as observed in previous studies (Ben-David et al. (2010); Passelègue et al. (2016), and references therein). Once the rupture fully propagated along the interface, the two sides of the fault started behaving like rigid blocks slipping one against the other, as shown by the evolution of the macroscopic slip and the cessation of measured acceleration motions (Fig. 1b).

2.3. Linear elastic fracture mechanics and cohesive zone model

During stick-slip experiments, the onset of slip arises in the wake of a propagating rupture that generates an associated stress perturbation. LEFM has been shown to be a valid tool to describe such perturbations in the stress field by analogy with a propagating shear crack, which is expected to create a singular field, whose intensity can be described by the stress intensity factor (K_{II}), a quantity accounting for geometry and loading conditions (Irwin, 1957). The main assumption of this model is that all dissipative processes occurring close to the crack tip must be concentrated in one point. The Cohesive Zone Model (CZM) regularizes the stress singularity by introducing a cohesive zone of finite dimension, x_c, where shear stress continuously decreases from a peak at the crack tip, τ_p, down to a constant residual value, τ_r (e.g., Poliakov et al. (2002)). The two quantities which control this model are x_c and the stress drop over which the dissipation occurs.

Both LEFM and CZM allow for an estimate of the fracture energy related to the propagation of the rupture, by imposing an equilibrium between the energy release rate and the fracture en-

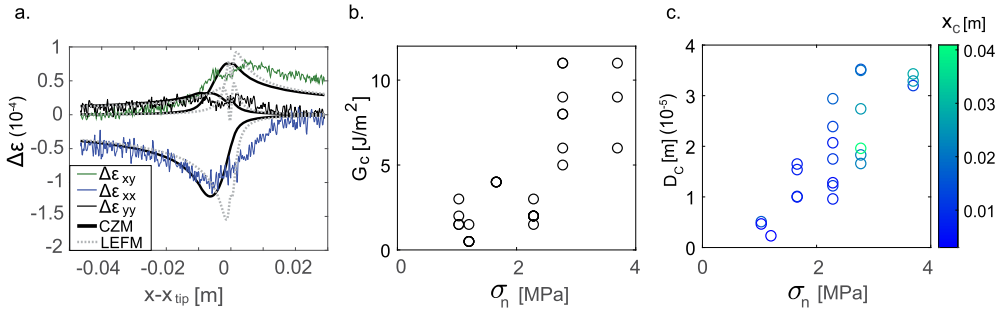

Fig. 2. a. Example of strain variation evolution during one rupture event ($\Delta\varepsilon_{xx}$, $\Delta\varepsilon_{yy}$, $\Delta\varepsilon_{xy}$). Theoretical predictions from CZM (in black) and LEFM (dashed gray) are plotted as well. b. Evolution of fracture energy inverted (from CZM) for all the studied rupture events for increasing applied normal load. c. Critical distance (D_c) evolution for all the studied rupture events with applied normal load, obtained by making use of cohesive zone (x_c) inverted through CZM.

ergy that respectively depends on K_{II} and (x_c, $\tau_p - \tau_r$) as detailed in the Supplemental Material. These two models were adopted, given their widespread use in recent experimental studies performed under similar conditions (Svetlizky and Fineberg, 2014; Bayart et al., 2016; Kammer and McLaskey, 2019).

3. Experimental results

3.1. Estimation of the fracture energy

Dynamic strain perturbations recorded at the vicinity of the rupture tip were compared to theoretical predictions, using both CZM (Poliakov et al., 2002; Kammer and McLaskey, 2019) and LEFM (Svetlizky and Fineberg, 2014) (Supplementary material). The LEFM solution was fitted through a least-squares method, by adjusting a single parameter, K_{II}, while the CZM solution was fitted by adjusting two parameters ($\tau_p - \tau_r$) and x_c (Fig. 2a). Both LEFM and CZM predictions output comparable values of G_c. This inversion was done for several events occurring at different applied normal loads (Fig. 2b, Table S1). As expected from previous studies (Okubo and Dieterich, 1984; Bayart et al., 2016), G_c increases with increasing applied normal load, due to an increase of contact area between the two surfaces. The values found ranged between 0.5 and 11 J/m^2, in agreement with previous estimates (Svetlizky and Fineberg, 2014; Bayart et al., 2016). Our results suggest that the cohesive zone (inverted from CZM) increases with the initial applied normal stress, with values ranging from 1 to 10 mm at 0.2 and 4 MPa applied normal stress, respectively (Fig. 2c). Note that for events presenting small values of x_c, CZM predictions collapse to those of LEFM, as expected theoretically and previously observed (Svetlizky and Fineberg, 2014). Finally, using our estimates of x_c, a characteristic slip-weakening distance was estimated as (Palmer and Rice, 1973)

$$D_c = x_c\, 4\,(1-\nu)\,(\tau_p - \tau_r)\,/\,\pi\,\mu. \qquad (2)$$

D_c increases with the initial normal stress from a few microns at the lowest stress tested to tens of microns at ≈ 4 MPa normal stress (Fig. 2c.), in agreement with previous studies (Ohnaka, 2003; Passelègue et al., 2016).

3.2. Comparison to local slip measurements

The values of fracture energy and frictional parameters inverted from CZM can be compared to the local evolution of stress versus slip. First of all, using the local strain tensor and the material's elastic properties, under the assumption of plain strain conditions, the shear stress evolution (τ) during instability was computed at 1 mm from the fault. Secondly, the strain measurements were used to compute the local slip induced along the fault during rupture propagation. The particle velocity was estimated from the strain component parallel to the slip direction, following $\dot{u}_x = -C_f \varepsilon_{xx}$ (Svetlizky and Fineberg, 2014). Then, local fault slip was obtained by integrating $\dot{u}_x$ with respect to time. The latter was compared to the slip obtained from the calibrated accelerometers located along the fault, computed following $u_x = \iint_t a(x)\,dt$, with a the measured acceleration in m/s^2 and t the time during propagation. The evolution of slip during rupture propagation obtained from both strain gauges and accelerometers is comparable (Fig. S1). The final values of slip obtained in this way are also comparable to the macroscopic slip measured by the laser sensor, suggesting that strain gauges provide a robust estimate of the local slip during rupture propagation, excluding possible strain-induced waves reflection. The total displacement occurring on the fault was computed as $D(t) = 2u_x$, assuming a symmetric displacement across the fault, given the uniform far-field loading.

In agreement with the slip-weakening assumption used in CZM, the onset of slip is marked by a large stress release (around 0.5 MPa) within a small amount of slip (around 10 μm) (Fig. 3a), an outcome which is in good agreement with our estimates of D_c using equation (2). This abrupt weakening stage is followed by a second long-tailed weakening stage during which the stress decreases continuously with increasing slip, at a much lower rate. During the first weakening stage, 70% of the final stress drop is achieved in the first micrometers of slip (Fig. 3). During the second stage, the weakening continues at a lower rate until the arrest of dynamic slip, defined here as the time at which the rupture propagated through the entire fault. It is important to highlight that a steady state residual stress is not achieved at the scale of our experiments. While the first weakening stage is predicted by CZM at the strain gauge locations (Fig. 3b), this long-tailed weakening is not expected to occur from the model, suggesting that at the scale of our experiments, fault weakening is more complex than expected from linear slip-weakening model (Palmer and Rice, 1973). This dual-scale weakening has been observed for decades in studies of engineering materials like concrete (Planas et al., 1997; Bažant, 2004), and is expected to give rise to a scale-dependent fracture energy, as it is observed from earthquakes scaling law (Madariaga, 2009).

3.3. Comparison between fracture energy, near-tip and long-tailed breakdown work

Keeping these last observations in mind, we now assume that the evolution of stress and slip estimated using the strain gauges located at 1 mm from the fault are representative of the real motions occurring along the fault during rupture propagation. This assumption seems robust since (i) the slip inverted from strain gauges at 1 mm from the fault is comparable to the one measured by the accelerometers and the laser sensor, (ii) the evolution

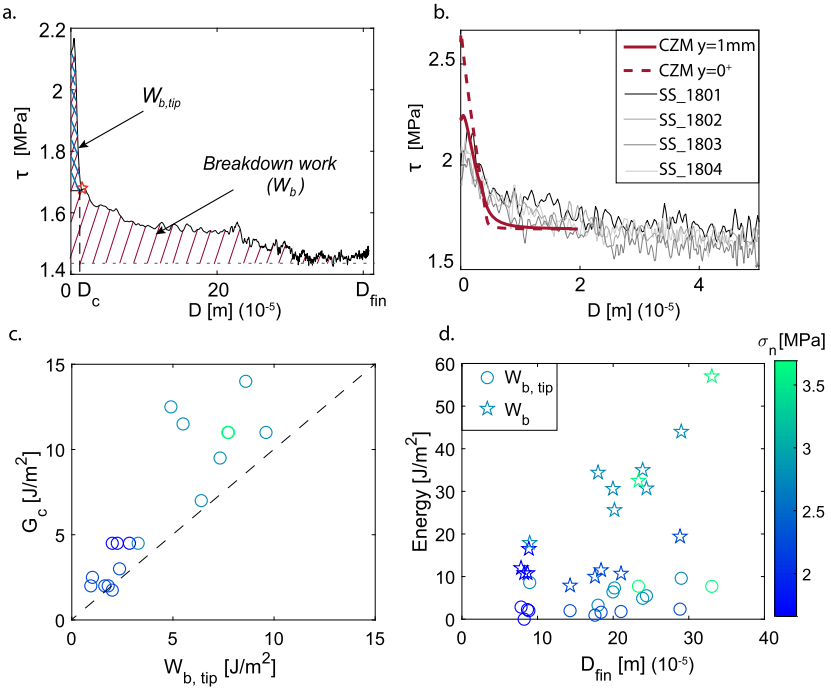

Fig. 3. a. Evolution of shear stress with fault slip for a specific rupture event. The area in blue represents the near tip breakdown work ($W_{b,tip}$), the one in red the overall breakdown work (W_b). b. Theoretical predictions from CZM corresponding to a distance of 1 mm from the fault (solid red line) and of 0^+ mm (dashed red line) plotted with the experimental curves. c. Comparison between fracture energy obtained from theoretical inversions (G_c Fig. 2) and $W_{b,tip}$. d. Evolution of $W_{b,tip}$ and W_b with applied normal load and associated final slip.

of the stress 1 mm away from the fault is close to the evolution of the stress on the fault, particularly in terms of energy dissipated (Fig. 3b). In general, off-fault shear stress is similar to that on the fault when it is measured at distances much smaller than the size of the cohesive zone, which is verified here.

The estimates of D_c, obtained from equation (2), allowed us to differentiate two principal weakening stages and to compute the energy dissipated during each of them. The energy dissipated at the crack tip, also known as the edge-localized dissipation (Barras et al., 2020), was computed for each event as $W_{b,tip} = \int_0^{D_c} (\tau(D) - \tau(D_c))\, dD$, using the measured shear stress τ. These values are in good agreement with G_c estimates obtained from the direct inversion of the strain perturbations shown above (Fig. 3c), showing that our near-fault stress measurements can be considered representative of on-fault stress, and, once more, that dynamic fracture mechanics is able to describe the onset of frictional sliding.

Secondly, the total dissipated energy resulting from the full stress evolution (i.e. breakdown work) was computed following

$$W_b = \int_0^{D_m} (\tau(D) - \tau(D_m))\, dD \tag{3}$$

where D_m corresponds to the value of slip for which the stress is minimum (τ_{min}) during rupture propagation. In our experiments D_m coincides with the final displacement D_{fin}. The energy dissipated during the complete weakening processes ranges between 1 and 60 J/m^2, i.e. values that are two to six times greater than $W_{b,tip}$ and G_c. While G_c slightly increases with applied normal load, as discussed previously, W_b covers a much wider range of values, which present a clear dependence with the final slip (Fig. 3d). These observations suggest that contrary to the energy dissipated at the rupture tip, which can be considered as an emerging property of the rough contact problem (fault roughness, normal pressure), the energy dissipated during the second weakening stage is rather controlled by frictional dissipation and slip history, presenting features similar to the breakdown work derived from high-velocity friction experiments (Nielsen et al., 2016) and natural earthquakes (Abercrombie and Rice, 2005; Tinti et al., 2005; Cocco and Tinti, 2008).

4. Discussion

4.1. Theoretical stress intensity factor including long-tailed weakening

In our experiments, the prolonged weakening does not completely contribute to fracture energy. However, one may wonder how and at which scale the long-tailed weakening may control rupture dynamics. As a first step, we analyze theoretically the influence of the cohesive stress distribution acting behind the crack tip on the stress intensity factor, and examine how stress variations far from the rupture tip may actually contribute to tip dynamics.

Let us consider a semi-infinite straight crack nucleating at t=0 in an infinite elastic medium. The crack is loaded under anti-plane shear conditions with a constant uniform background stress τ_b. The propagation of the shear crack is resisted by cohesive frictional stresses $\tau_f(x,t)$. Following our experimental results, which provide evidence for a dual-scale weakening stage, the frictional stresses can be decomposed into the sum of three terms defined by (i) $\tau_{f,tip}(D(x,t))$ describing the near-tip weakening due to the local instantaneous slip D, (ii) $\tau_{f,tail}(D(x,t))$ associated to the long-tailed weakening, and (iii) the uniform residual stresses $\tau_{r,tail}$ at large slip. The stress intensity factor resulting of the evolution of stress with slip is written as (Kostrov, 1966)

$$k_{tot}(x_{tip}, C_f, t) = \beta_s(C_f) \int_0^{C_s t} \left[\tau_b(x_{tip} - r) - \tau_{r,tail}\right] \frac{dr}{\sqrt{r}}$$

$$- \beta_s(C_f) \int_0^{C_s t} \tau_{f,tip}\left(D(x_{tip} - r, t - r/C_s)\right) \frac{dr}{\sqrt{r}} \quad (4)$$
$$- \beta_s(C_f) \int_0^{C_s t} \tau_{f,tail}\left(D(x_{tip} - r, t - r/C_s)\right) \frac{dr}{\sqrt{r}},$$

where x_{tip} is the position of the rupture tip, $\beta_s(C_f) = \sqrt{\frac{2}{\pi}}\sqrt{1 - C_f/C_s}$ is a universal pre-factor depending of the rupture velocity C_f, r is the longitudinal distance to the rupture tip, and C_s is the shear wave velocity of the material.

The presence of cohesion behind the rupture tip implies that the stresses remain non-singular at the rupture tip ($k_{tot} = 0$). Assuming this, the total stress intensity factor can then be rewritten from equation (4) as

$$k_{tot}(x_{tip}, C_f, t) = k(x_{tip}, C_f) - k_{tip}(x_{tip}, C_f, t) - k_{tail}(x_{tip}, C_f, t) = 0, \quad (5)$$

where k is the first term of the right hand side of equation (4) and corresponds to the stress intensity factor that emerges when all weakenings are occurring within an infinitesimally small region behind the rupture tip, k_{tip} is the second term of the right hand side of equation (4) and corresponds to the contribution of the near-tip weakening frictional stresses, and k_{tail} is the third term of the right hand side of equation (4) and relates to the frictional stresses that weaken far from the rupture tip.

The terms of equation (5) are very different by nature. Indeed, since $\tau_{f,tip}$ is nonzero only in a small region of dimension $x_{c,tip}$ near the tip, k_{tip} is independent from time and can be written as a velocity-dependent "cohesion modulus" $k_{tip}(C_f)$ (i.e., dynamic toughness) (Kostrov, 1966). On the contrary, k_{tail}, the contribution of the long-tailed weakening to the total stress intensity factor k_{tot} relates to the distribution of frictional stress $\tau_{f,tail}$ in a larger region of size $x_{c,tail} \gg x_{c,tip}$ with some delay due to the wave-mediated nature of the stress transfer. As such, the breakdown work of equation (3) depends only on the spatial distribution of slip ($D(x)$), while the energy absorbed at the rupture tip is function of the spatio-temporal evolution of slip $D(x,t)$ near the propagating front and strongly depends on the rupture velocity.

One may then distinguish three characteristic regimes depending on the rupture length (L) with respect to the characteristic cohesive zone sizes.

Regime (i): $x_{c,tip} < L < x_{c,tail}$. $\tau_{f,tail}$ can be considered locally constant outside of $x_{c,tip}$. The stress singularity in front of the rupture tip is dominated by $\propto k_{LEFM}/\sqrt{r}$. In this regime $k_{LEFM} = (k - k_{tail}) = k_{tip}(C_f)$, and the dynamic energy balance can be written following (Freund (1998) chap. 5):

$$G = \frac{k_{LEFM}(x_f, C_f)^2}{2\mu\sqrt{(1 - C_f^2/C_s^2)}} = \frac{k_{tip}(C_f)^2}{2\mu\sqrt{(1 - C_f^2/C_s^2)}} = G_{c,tip}, \quad (6)$$

meaning that the energy dissipated to make the rupture propagate corresponds to the near-tip fracture energy only.

Regime (ii): $L \approx x_{c,tail}$. Once the long tailed weakening initiates, the stress state in the vicinity of the rupture tip results from the combination of background stress and long tailed frictional stress following $\propto (k - k_{tail}) = k_{tip}(C_f)$. However, in this intermediate case no clear residual frictional stress is achieved during propagation. Yet, if there is a clear separation of scales between $x_{c,tip}$ and $x_{c,tail}$, the energy balance at the rupture tip is well-approximated by equation (6).

Regime (iii): $L \gg x_{c,tail}$ (i.e., both the near-tip and long-tailed weakening occur within a small region behind the rupture tip). A well defined residual stress $\tau_{r,tail}$ is reached behind the rupture tip. In this case, both types of weakening control the rupture dynamics ($k_{LEFM} = k_{tip}(C_f) + k_{tail}(C_f)$). The energy balance reads

$$G = \frac{k_{LEFM}(C_f)^2}{2\mu\sqrt{(1 - C_f^2/C_s^2)}} = G_{c,tip} + G_{c,tail}. \quad (7)$$

In this case, the fracture energy measured from the tip stress singularity equals the complete breakdown work, potentially much larger than the fracture energy associated with the near-tip weakening.

Moreover, rupture velocity can influence such regimes, enhancing the contribution of long-tailed weakening to the rupture tip for low C_f (i.e., the lower the rupture velocity, the shorter the time needed for stress waves traveling at C_s to catch up with the propagating tip). For short crack lengths or near-C_s ruptures, crack dynamics are dominated by the near-tip weakening only, and the total breakdown work can be much larger than fracture energy. This is what we observed in our experiments, where probably our finite fault length was too small to observe contributions of the long-tailed weakening. For large rupture lengths or lower rupture velocities, breakdown work and fracture energy are equal and crack dynamics are controlled by the total energy. The transition between these simple regimes is further investigated with numerical simulations in the next section.

4.2. Modeling frictional rupture with a dual-scale slip-weakening law

Once the rupture length (L_f) reaches a sufficient size $L_f \gg x_{c,tail}$, two scenarios are admissible in light of the small-scale yielding requirement (i.e., dissipative phenomena limited to a region much smaller than the dimensions of the system). The rupture tip dynamics is driven either by the first or the second weakening stage depending on the rupture history (total length and speed). To shed light on the realization of these two scenarios, we conduct numerical simulations of frictional ruptures (see Supplementary Materials for details on the numerical method) driven by slip-weakening friction laws with different weakening length scales. For simplicity, only mode III ruptures were studied in order to avoid rupture propagation velocities larger than the shear wave velocity, which would add unnecessary complexity to our results. The reference case consists of a linear slip-weakening law defined by a peak stress τ_p, residual stress $\tau_r = 0.8\tau_p$ and a slip-weakening distance $D_{c,tip}$. The tested case consists of a dual-scale slip-weakening law, that matches the reference case in the first stage, but which is followed by a second long-tailed weakening stage (Fig. 4 inset) allowing a larger stress release up to a final residual stress $\tau_{r,tail} = 0.1\tau_p$ over a weakening distance $D_{c,tail} = 50D_{c,tip}$ (details can be found in the Supplementary Material). In both cases, the initial background stress (τ_b) along the fault was set to a uniform value, and rupture nucleation was triggered by imposing an elevated stress patch $\tau_{b,nucl}$ 5% above τ_p in a small region at the center of the modeled fault.

During the propagation phase of the rupture, the numerical results obtained for the reference slip-weakening law show a symmetric crack-like rupture propagating across the interface, with an increase in stress and slip velocity occurring near the tip of the crack (Figs. 4a and 4c). To further investigate the dynamics at the rupture tip, the increase in slip velocity at the vicinity of the crack tip was fitted with LEFM predictions (Fig. 4e) following (Barras et al., 2020)

$$v(r = x - x_{tip}, \theta = \pi, C_f) \approx \frac{K_{III}^2 C_f}{\sqrt{2\pi(x - x_{tip})}\mu\alpha_s(C_f)} \quad (8)$$

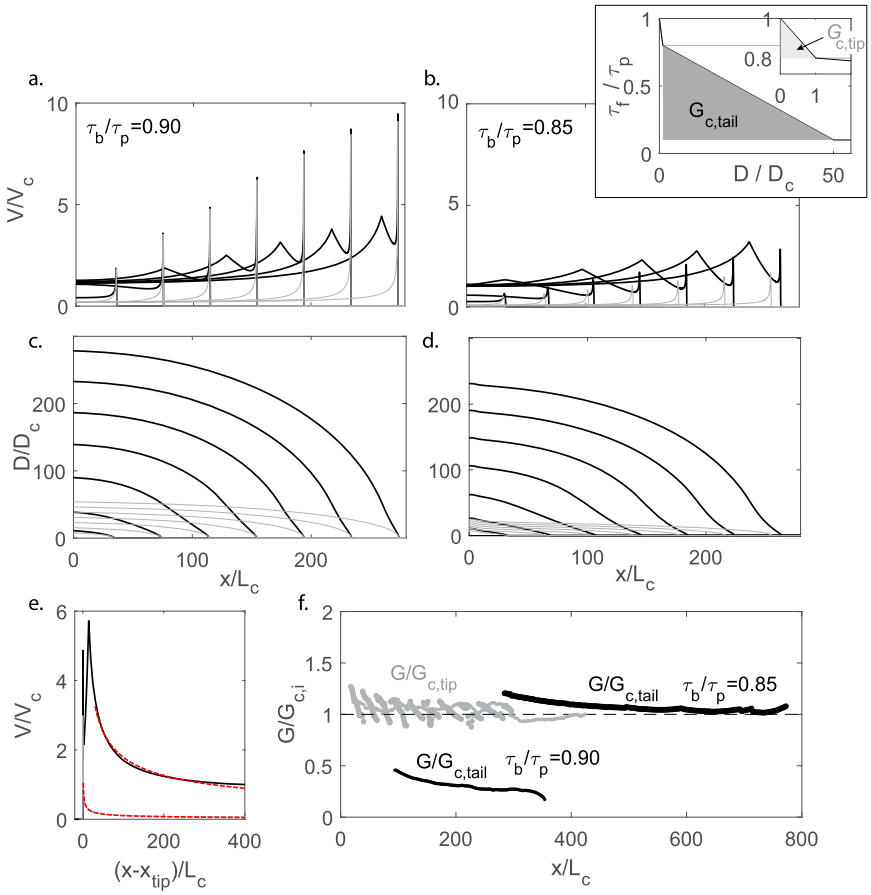

Fig. 4. a., b. Normalized slip rate (V/V_c) evolution along fault length for simple (in gray) and dual-scale (in black) slip-weakening laws, respectively for ($\tau_b/\tau_p = 0.90$) and ($\tau_b/\tau_p = 0.85$). $V_c = \mu C_s/\tau_p$ is the critical slip rate. Inset: constitutive laws used for the numerical simulations. In gray the simple slip-weakening law describing the first weakening stage observed, in black the dual-scale slip-weakening law describing both first and second weakening with associated fracture energies ($G_{c,tip}$, $G_{c,tail}$). c.,d. Slip profile evolution along fault length for both weakening laws respectively for ($\tau_b/\tau_p = 0.90$) and ($\tau_b/\tau_p = 0.85$). e. Example of the fit of slip rate profiles with theoretical predictions (in dashed red) for the simple weakening case and dual-weakening case with $\tau_b/\tau_p = 0.85$. f. Energy release rate evolution with rupture size for the simple weakening law normalized by fracture energy $G_{c,tip}$ (in gray) and for the dual-scale weakening law normalized by fracture energy $G_{c,tail}$ (in black).

where K_{III} is the stress intensity factor, r, θ is a polar coordinate system moving with the rupture tip, and $\alpha_s(C_f) = \sqrt{1 - C_f^2/C_s^2}$. The best fit outputs the solution for the stress intensity factor, which is directly related to the energy release rate following

$$G = \frac{K_{III}^2}{2\mu\alpha_s(C_f)}. \tag{9}$$

The latter is used to study the near-tip energy balance controlling the dynamics of the rupture tip during its propagation (Barras et al., 2020). This analysis demonstrates that during the rupture propagation driven by the simple slip-weakening law, the energy balance $G = G_{c,tip}$ is systematically respected, independently of the rupture length (Fig. 4f). Note that small variations in the energy release rate are observed during the crack propagation, due to the uncertainties on the estimate of the rupture velocity and sharp variations of $1/\alpha_s(C_f)$ near $C_f \simeq C_s$. This result confirms that the energy release rate at the crack tip is controlled by the near-tip fault weakening, as expected theoretically (Irwin, 1957; Barras et al., 2020).

Interestingly, the results obtained for the dual-scale weakening law show the aforementioned different scenarios as function of the background stress. The overall effect of the used dual-scale slip-weakening law is reflected in a larger slip and slip velocity in the central part of the crack (Fig. 4), which lead to the emergence of a second increase in slip velocity traveling behind the slip velocity peak characterizing the rupture propagation front. Note that such kind of rupture fronts presenting two successive increases in slip velocity have been recently recorded during rupture experiments presenting low rupture velocities, i.e., low initial normal stress, (Berman et al., 2020). For frictional rupture under high background stress (i.e., $\tau_b = 0.9\tau_p$), the nucleated rupture driven by the first-weakening mechanism ($G = G_{c,tip}$) keeps accelerating such that it is barely perturbed by the effect of the long-tailed weakening. An example of such dynamics is presented in Fig. 4a and shows a propagation very similar to the equivalent simple slip-weakening setup. Moreover, the increase in the slip velocity profile generated by the long-tailed weakening leads to an associated energy release rate much smaller than $G_{c,tail}$, confirming that it is not controlling rupture propagation (Fig. 4f). Conversely, if the background stress is smaller (i.e., $\tau_b = 0.85\tau_p$), the increase of slip rate generated by the second-weakening stage can reach the leading front and accelerate the rupture further. Such situation is shown in Fig. 4c that highlights how the rupture is now propagating faster than in the case of simple slip-weakening law. The inverted value of G from the slip velocity profile is now balancing $G_{c,tail}$, confirming that the long-tailed weakening mechanism is driving the rupture. Remarkably, for the slip-weakening model used in these simulations, dynamic fracture arguments can be used to predict the critical level of background stress τ_b^* that controls the observed transition between ($\tau_b > \tau_b^*$) and ($\tau_b < \tau_b^*$) (see the details in Supplemental material).

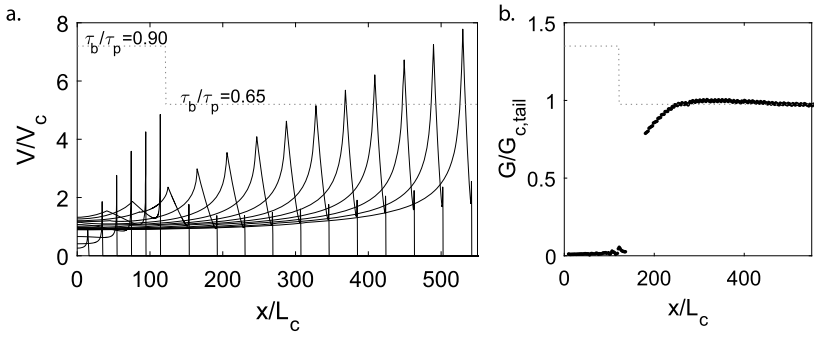

Fig. 5. a. Slip rate evolution with rupture length in presence of a stress barrier with rupture propagation controlled by the dual-scale weakening law. The initial background stress distribution is presented by the grey dashed line. b. Energy release rate evolution with rupture length. Once overpassed the stress barrier, the energy release rate jumps to the value of fracture energy describing the long-tailed weakening $G = G_{c,tail}$ (i.e., rupture dynamics controlled by the long-tailed weakening).

4.3. Contributions of long-tailed weakening in presence of a stress heterogeneity

We showed how the long-tailed weakening induces larger slip and higher slip velocities away from the rupture tip. One consequence of this additional weakening could result in helping to overcome stress heterogeneities distributed along faults. To study this specific case, we impeded rupture acceleration by introducing a low stressed area at a distance $x/L_c = 120$ from the center of the fault, with $L_c = \mu Dc/\tau_p$. The background stress, set initially at $\tau_b/\tau_p = 0.90$ was decreased to $\tau_b/\tau_p = 0.65$ in the outer region of the space domain. Under these conditions, once the rupture nucleates, it propagates generating two slip velocity peaks (Fig. 5a), in a similar way to the case without a stress barrier. However, due to the decrease of background stress, which is now much smaller than the residual stress associated to the first weakening $\tau_r = 0.8\tau_p$, the rupture tip is momentarily stopped (since $G < G_{c,tip}$) at the barrier location. As time grows, the enhanced stress drop due to the prolonged weakening near the fault center reaches the rupture tip, promoting the propagation of the rupture across the barrier, which is observed as a second (large) peak slip rate takes over the rupture. The second weakening subsequently controls the complete rupture dynamics, following $G = G_{c,tail}$ (Fig. 5b). These observations suggest that the large amount of slip induced by the long-tailed weakening allows the rupture to overcome zones of lower background stress that would normally stop the rupture controlled by the near-tip weakening only.

While a small amount of energy is sufficient to nucleate and propagate a frictional rupture along fault interfaces, the presence of stress heterogeneities along a fault are expected to obstruct the propagation of ruptures induced by a rapid but limited frictional weakening. However, substantial weakening mechanisms activated at larger critical distances achieved in the central part of the crack can enhance the propagation of seismic rupture through regions of lower background stress, and control afterwards the dynamics of the rupture. It emerges a possible scale dependence in the dynamics of rupture controlled by multiple weakening stages, meaning that cracks presenting large values of fracture energy can propagate due to the activation of slip on smaller cracks presenting lower values of fracture energy (i.e., enhancing propagation). This seems in agreement with recent experimental results highlighting that frictional instabilities are initiated by small events growing and cascading up into a much larger rupture (McLaskey and Lockner, 2014). This cascade of weakening mechanisms is also consistent with the sequence of deformation processes reported in fields observation of exhumed fault zones (Incel et al., 2019). Following our interpretation, the origin of breakdown work inverted from seismological observations could be related to energy dissipated through frictional weakening mechanisms, as suggested by Cocco et al. (2006), rather than to the one dissipated near-tip (i.e., fracture energy of the interface). In fact, while the onset of friction is described by standard fracture processes, as stated in previous studies (Svetlizky and Fineberg, 2014), earthquake motions could be related to frictional weakening processes at the scale of crustal faults, which are expected to promote large values of breakdown work due to the activation of thermal processes during seismic slip (Di Toro et al., 2011), and to present a clear dependence with slip, as observed for natural earthquakes (Abercrombie and Rice, 2005; Nielsen et al., 2016).

5. Conclusions

Our results presented above highlight that:

i) A two-stage fault weakening is observed experimentally during frictional rupture propagation. A first rapid decay occurs within few microns of slip (ascribed to the critical slip distance D_c), followed by a long-tailed weakening, for which a steady state residual strength is not achieved at the scale of our experiments.
ii) The energy dissipated at the rupture tip is associated with the first weakening stage, defined here as the fracture energy of the interface G_c. This energy is the one controlling the onset of frictional rupture as already shown (Svetlizky and Fineberg, 2014). The energy dissipated during the long-tailed weakening corresponds to the breakdown work, which describes frictional weakening processes occurring at the interface during seismic slip.
iii) The derivation of the energy balance through the analysis of the stress intensity factors shows that further weakening, occurring once fracture energy is dissipated, will produce an additional energy release. This is expected to grow with time as more and more slip is achieved, enhancing the energy release rate at the rupture tip and facilitating rupture propagation.
iv) Numerical simulations reveal the interplay between two successive weakening mechanisms represented by a dual-scale slip-weakening law. The rapid near-tip weakening mechanism controls the propagation dynamics in regions of high background stress ($\tau_b > \tau_b^*$) where rupture is expected to nucleate. Once the nucleated rupture has generated sufficient slip to activate the second weakening mechanism, the resulting long-tail dissipation is able to drive the rupture further into portions of the fault with lower background stress ($\tau_b < \tau_b^*$) and across stress barriers.

Our results provide insights to interpret the scaling relationship of breakdown work with slip, already widely observed for mining, induced seismicity, laboratory earthquakes and natural

earthquakes. At first sight, the breakdown work of natural earthquakes appears to increase linearly with seismic slip (Abercrombie and Rice, 2005; Tinti et al., 2005; Nielsen et al., 2016; Selvadurai, 2019). However, single populations of smaller earthquakes ($M_w < 5$) seem to follow independent power law (with exponent $\sim$2) relationships, compatible with linear slip-weakening behavior (for details, please refer to the Supplementary Material and Fig. S4). These successive power-two relationships suggest that earthquakes spanning several ranges of magnitudes could exhibit different weakening processes, activated at different length-scales. In consequence, the amount of breakdown work generated during rupture propagation would be the result of the final slip and of the initial shear stress acting along the fault (i.e. of the stress drop), rather than the final rupture length (as for a circular crack model). Of course, in nature, the evolution of stress with slip is expected to deviate from the simple linear slip-weakening behavior assumed for simplicity in this work, which is expected to modify the slip dependence of the breakdown work, as observed in recent studies (Viesca and Garagash, 2015; Lambert and Lapusta, 2020). However, the activation of different weakening mechanisms with increasing slip suggests that while natural earthquakes might be expected to initiate like classical shear cracks, subsequent frictional weakening at the scale of the entire rupture can help the earthquake to grow further into lowly-stressed regions of the fault and across barriers.

CRediT authorship contribution statement

F.P.: Conceptualization, Data Production, Numerical Simulations, Data Analysis, Theoretical Analysis, Writing – Original Draft.

F.X.P.: Conceptualization, Data Production, Numerical Simulations, Data Analysis, Theoretical Analysis, Writing – Original Draft.

N.B.: Development of the numerical model, Numerical Simulations, Development of the Theoretical derivation, Writing – Reviewing and Editing.

F.B.: Development of the numerical model, Numerical Simulations, Development of the Theoretical derivation, Writing – Reviewing and Editing.

M.L.: Development of the Theoretical derivation, Data Analysis, Writing – Reviewing and Editing.

M.V.: Conceptualization, Data Analysis, Writing – Reviewing and Editing.

Declaration of competing interest

The authors declare that they have no known competing financial interests or personal relationships that could have appeared to influence the work reported in this paper.

Data availability

The data from this paper are available at the following address: https://doi.org/10.5281/zenodo.6200886.

Acknowledgements

F.P., F.X.P. and M.V. would like to thank Jay Fineberg and Jean-François Molinari for helpful discussions. F.P. and F.X.P. thank Paul Selvadurai for sharing data set on natural seismicity. F.P., M.L. and M.V. acknowledge support by the European Research Council Starting Grant project 757290-BEFINE. F.B. acknowledges support of the Swiss National Science Foundation through the fellowship No. P2ELP2/188034. The authors thank Elisa Tinti and an anonymous reviewer for their constructive comments which improved the manuscript.

Appendix A. Supplementary material

Supplementary material related to this article can be found online at https://doi.org/10.1016/j.epsl.2022.117442.

References

Abercrombie, R.E., Rice, J.R., 2005. Can observations of earthquake scaling constrain slip weakening? Geophys. J. Int. 162 (2), 406–424. https://doi.org/10.1111/j.1365-246X.2005.02579.x.

Barras, F., Aldam, M., Roch, T., Brener, E.A., Bouchbinder, E., Molinari, J.F., 2020. The emergence of crack-like behavior of frictional rupture: edge singularity and energy balance. Earth Planet. Sci. Lett. 531, 115978. https://doi.org/10.1016/j.epsl.2019.115978.

Bayart, E., Svetlizky, I., Fineberg, J., 2016. Fracture mechanics determine the lengths of interface ruptures that mediate frictional motion. Nat. Phys. 12, 166–170. https://doi.org/10.1038/NPHYS3539.

Bažant, Z.P., 2004. Scaling theory for quasibrittle structural failure. Proc. Natl. Acad. Sci. USA 101 (37), 13400–13407. https://doi.org/10.1073/pnas.0404096101.

Ben-David, O., Cohen, G., Fineberg, J., 2010. The dynamics of the onset of frictional slip. Science 330 (6001), 211–214. https://doi.org/10.1126/science.1194777.

Berman, N., Cohen, G., Fineberg, J., 2020. Dynamics and properties of the cohesive zone in rapid fracture and friction. Phys. Rev. Lett. 125 (12), 125503. https://doi.org/10.1103/PhysRevLett.125.125503.

Brantut, N., Viesca, R.C., 2017. The fracture energy of ruptures driven by flash heating. Geophys. Res. Lett. 44 (13), 6718–6725. https://doi.org/10.1002/2017GL074110.

Brener, E.A., Bouchbinder, E., 2021. Unconventional singularities and energy balance in frictional rupture. Nat. Commun. 12, 2585. https://doi.org/10.1038/s41467-021-22806-9.

Causse, M., Dalguer, L.A., Mai, P.M., 2014. Variability of dynamic source parameters inferred from kinematic models of past earthquakes. Geophys. J. Int. 196 (3), 1754–1769. https://doi.org/10.1093/gji/ggt478.

Cocco, M., Spudich, P., Tinti, E., 2006. On the mechanical work absorbed on faults during earthquake ruptures. Geophys. Monogr. 170 (1), 237–254. https://doi.org/10.1029/170GM24.

Cocco, M., Tinti, E., 2008. Scale dependence in the dynamics of earthquake propagation: evidence from seismological and geological observations. Earth Planet. Sci. Lett. 273 (1–2), 123–131. https://doi.org/10.1016/j.epsl.2008.06.025.

Cornelio, C., Passelègue, F.X., Spagnuolo, E., Di Toro, G., Violay, M., 2020. Effect of fluid viscosity on fault reactivation and coseismic weakening. J. Geophys. Res., Solid Earth 125 (1), e2019JB018883. https://doi.org/10.1029/2019JB018883.

Di Toro, G., Han, R., Hirose, T., De Paola, N., Nielsen, S., Mizoguchi, K., Ferri, F., Cocco, M., Shimamoto, T., 2011. Fault lubrication during earthquakes. Nature 471 (7339), 494–499. https://doi.org/10.1038/nature09838.

Freund, L.B., 1998. Dynamic Fracture Mechanics. Cambridge University Press.

Galis, M., Ampuero, J.P., Mai, P.M., Cappa, F., 2017. Induced seismicity provides insight into why earthquake ruptures stop. Sci. Adv. 3 (12). https://doi.org/10.1126/sciadv.aap7528.

Incel, S., Schubnel, A., Renner, J., John, T., Labrousse, L., Hilairet, N., Freeman, H., Wang, Y., Renard, F., Jamtveit, B., 2019. Experimental evidence for wall-rock pulverization during dynamic rupture at ultra-high pressure conditions. Earth Planet. Sci. Lett. 528, 115832. https://doi.org/10.1016/j.epsl.2019.115832.

Irwin, G.R., 1957. Analysis of stresses and strains near the end of a crack transversing a plate. Trans. ASME, Ser. E, J. Appl. Mech. 24, 361–364.

Johnson, T.L., Scholz, C.H., 1976. Dynamic properties of stick-slip friction of rock. J. Geophys. Res. 81 (5), 881–888. https://doi.org/10.1029/jb081i005p00881.

Kammer, D.S., McLaskey, G.C., 2019. Fracture energy estimates from large-scale laboratory earthquakes. Earth Planet. Sci. Lett. 511, 36–43. https://doi.org/10.1016/j.epsl.2019.01.031.

Kammer, D.S., Radiguet, M., Ampuero, J.P., Molinari, J.F., 2015. Linear elastic fracture mechanics predicts the propagation distance of frictional slip. Tribol. Lett. 57 (3). https://doi.org/10.1007/s11249-014-0451-8. arXiv:1408.4413.

Kanamori, H., 1977. The energy release in great earthquakes. J. Geophys. Res. 82 (20). https://doi.org/10.1029/JB082i020p02981.

Kanamori, H., Brodsky, E.E., 2004. The physics of earthquakes. Rep. Prog. Phys. 67 (8), 1429–1496. https://doi.org/10.1088/0034-4885/67/8/R03.

Ke, C.Y., McLaskey, G.C., Kammer, D.S., 2020. The earthquake arrest zone. Geophys. J. Int. 224 (1), 581–589. https://doi.org/10.1093/gji/ggaa386.

Ke, C.Y., McLaskey, G.C., Kammer, D.S., 2022. Earthquake breakdown energy scaling despite constant fracture energy. Nat Commun. 13, 1005. https://doi.org/10.1038/s41467-022-28647-4.

Kostrov, B.V., 1966. Unsteady propagation of longitudinal shear cracks. J. Appl. Math. Mech. 30 (6), 1241–1248. https://doi.org/10.1016/0021-8928(66)90087-6.

Lambert, V., Lapusta, N., 2020. Rupture-dependent breakdown energy in fault models with thermo-hydro-mechanical processes. Solid Earth 11 (6), 2283–2302. https://doi.org/10.5194/se-11-2283-2020.

Madariaga, R., 2009. Earthquake scaling laws. In: Meyers, A. (Ed.), Encyclopedia of Complexity and Systems Science. Springer, New York, p. 10370.

McLaskey, G.C., Lockner, D.A., 2014. Preslip and cascade processes initiating laboratory stick slip. J. Geophys. Res., Solid Earth 119 (8), 6323–6336. https://doi.org/10.1002/2014JB011220.

Nielsen, S., Spagnuolo, E., Violay, M., Smith, S., Di Toro, G., Bistacchi, A.G., 2016. Fracture energy, friction and dissipation in earthquakes. J. Seismol. 20 (4), 1187–1205. https://doi.org/10.1007/s10950-016-9560-1.

Ohnaka, M., 2003. A constitutive scaling law and a unified comprehension for frictional slip failure, shear fracture of intact rock, and earthquake rupture. J. Geophys. Res. 108 (B2). https://doi.org/10.1029/2000JB000123.

Ohnaka, M., Yamashita, T., 1989. A cohesive zone model for dynamic shear faulting based on experimentally inferred constitutive relation and strong motion source parameters. J. Geophys. Res. 94 (B4), 4089–4104. https://doi.org/10.1029/JB094iB04p04089.

Okubo, P.G., Dieterich, J.H., 1984. Effects of physical fault properties on frictional instabilities produced on simulated faults. J. Geophys. Res., Solid Earth 89 (B7), 5817–5827. https://doi.org/10.1029/JB089iB07p05817.

Palmer, A.C., Rice, J.R., 1973. The growth of slip surfaces in the progressive failure of over-consolidated clay. Proc. R. Soc. Lond. Ser. A, Math. Phys. Sci. 332 (1591), 527–548. https://doi.org/10.1098/rspa.1973.0040.

Passelègue, F.X., Almakari, M., Dublanchet, P., Barras, F., Fortin, J., Violay, M., 2020. Initial effective stress controls the nature of earthquakes. Nat. Commun. 11 (1), 1–8. https://doi.org/10.1038/s41467-020-18937-0.

Passelègue, F.X., Schubnel, A., Nielsen, S., Bhat, H.S., Deldicque, D., Madariaga, R., 2016. Dynamic rupture processes inferred from laboratory microearthquakes. J. Geophys. Res., Solid Earth 121 (6), 4343–4365. https://doi.org/10.1002/2015JB012694.

Planas, J., Guinea, G.V., Elices, M., 1997. Generalized size effect equation for quasibrittle materials. Fatigue Fract. Eng. Mater. Struct. 20 (5), 671–687. https://doi.org/10.1111/j.1460-2695.1997.tb00300.x.

Poliakov, A.N.B., Dmowska, R., Rice, J.R., 2002. Dynamic shear rupture interactions with fault bends and off-axis secondary faulting. J. Geophys. Res. 107 (B11). https://doi.org/10.1029/2001JB000572.

Rubinstein, S.M., Cohen, G., Fineberg, J., 2004. Detachment fronts and the onset of dynamic friction. Nature 430, 1005–1009. https://doi.org/10.1038/nature02861.1.

Selvadurai, P.A., 2019. Laboratory insight into seismic estimates of energy partitioning during dynamic rupture: an observable scaling breakdown. J. Geophys. Res., Solid Earth 124 (11), 11350–11379. https://doi.org/10.1029/2018JB017194.

Seyler, C.E., Kirkpatrick, J.D., Savage, H.M., Hirose, T., Faulkner, D.R., 2020. Rupture to the trench? Frictional properties and fracture energy of incoming sediments at the Cascadia subduction zone. Earth Planet. Sci. Lett. 546, 116413. https://doi.org/10.1016/j.epsl.2020.116413.

Svetlizky, I., Fineberg, J., 2014. Classical shear cracks drive the onset of dry frictional motion. Nature 509 (7499), 205–208. https://doi.org/10.1038/nature13202.

Tinti, E., Spudich, P., Cocco, M., 2005. Earthquake fracture energy inferred from kinematic rupture models on extended faults. J. Geophys. Res., Solid Earth 110 (12), 1–25. https://doi.org/10.1029/2005JB003644.

Twardzik, C., Das, S., Madariaga, R., 2014. Inversion for the physical parameters that control the source dynamics of the 2004 Parkfield earthquake. J. Geophys. Res., Solid Earth 119 (9), 7010–7027. https://doi.org/10.1002/2014JB011238.

Venkataraman, A., Kanamori, H., 2004. Effect of directivity on estimates of radiated seismic energy. J. Geophys. Res. 109, 1–12. https://doi.org/10.1029/2003JB002548 (October 2003).

Viesca, R.C., Garagash, D.I., 2015. Ubiquitous weakening of faults due to thermal pressurization. Nat. Geosci. 8 (11), 875–879. https://doi.org/10.1038/ngeo2554.

Xu, S., Fukuyama, E., Yamashita, F., 2019. Robust estimation of rupture properties at propagating front of laboratory earthquakes. J. Geophys. Res. 124 (1), 766–788. https://doi.org/10.1029/2018JB016797.